Towards the Optimal Design of Support Structures for Laser Powder Bed Fusion-Based Metal Additive Manufacturing via Thermal Equivalent Static Loads

Subodh C. Subedi[1], **Ahmad Shahba**[2], **Mythili Thevamaran**[4], **Dan J. Thoma**[1,3,4,5], and **Krishnan Suresh** *[1,5]

[1]*Mechanical Engineering Department, University of Wisconsin-Madison, USA*

[2]*Technical Data Analysis Inc., Falls Church, VA, USA*

[3]*Material Science and Engineering Department, University of Wisconsin-Madison, USA*

[4]*Grainger Institute for Engineering, University of Wisconsin-Madison, USA*

[5]*Engineerting Physics Department, University of Wisconsin-Madison, USA*

Abstract

In laser powder bed fusion (LPBF)-based metal additive manufacturing, support structures play a crucial role in ensuring part-printability. However, support structures often consume significant amount of material, print-time and post-processing time. Furthermore, the optimal design of these support structures is challenging due to the transient nature of the LPBF process. Consequently, support structures are often sub-optimal, and are designed based on experience.

Here, we propose the concept of an *aggregate equivalent static load* (ESL) for the design of support structures. Starting with a simple transient simulation of the layer-wise LPBF build process, we extract the ESL at the end of each time step. An aggregate ESL is then computed for minimizing the thermal compliance of support structures, subjected to a volume constraint. The ESL concept is demonstrated here using truss-type support structures; however, it is equally applicable for other types of supports. Truss-type supports are generated using a novel greedy algorithm, and then the aggregate ESL strategy is applied to optimize the size of truss members. Numerical experiments are conducted to ascertain the self-consistency of the proposed method. The optimized cross-section areas of truss members are then converted to manufacturable designs, and sample parts are fabricated for validation.

*Corresponding email: ksuresh@wisc.edu

1 Introduction

Laser powder bed fusion (LPBF) is perhaps the most popular metal additive manufacturing process today, where a high energy laser beam selectively melts metal powder layer-by-layer. The ability to print complex geometries with high accuracy and repeatability, makes this technology a preferred choice for functional components. However, a central challenge in LPBF is efficient heat dissipation. The metal powder bed supports part layers against the effect of gravity, however, it exhibits less than 10% thermal conductivity, compared to their solid counterparts [1, 2], so cannot function as a thermal conduit. Consequently, any part-surface with surface normal inclined at or over a predefined threshold inclination angle (usually 45°with respect to the build direction) will require additional support structures for heat dissipation [3].

A typical part with commonly used block-type support structure is illustrated in Figure 1. Support structures consist of two distinct regions: support comb and support body. The support combs penetrate into the part for better anchorage and to reduce surface roughness [4]. The support body, constituting the bulk of support structures, serves as the heat transfer path from part to build surface, and provides additional structural strength. In addition, support structures reduce thermal deformation of the part, and prevent structural damage to the part during post-processing/removal from the build plate. Cutouts are often added into the support body for the ease of powder removal. The efficient dissipation of heat from melt pool reduces residual stresses [5–7], de-lamination [8], metal dross [9], and also improves micro-structural properties [7, 10–12]. Thus, a well-designed support structure is crucial in LPBF to ensure a successful build.

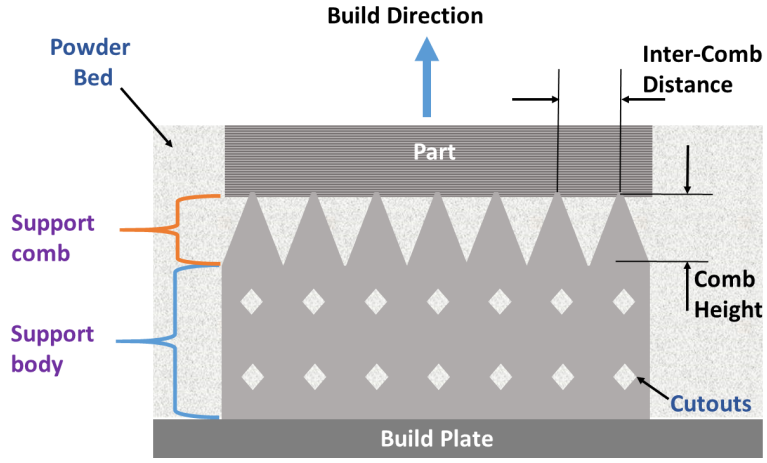

Figure 1: *Part build configuration with block-type support structures in LPBF.*

However, support structures often consume significant amount of material, print time, and post-processing time. Furthermore, due to the transient nature of the LPBF process, the optimal design of these support structures is non-trivial, and a systematic design strategy does not exist. This requires inclusion of part thermal history in determining the thermal behavior of part and supports during the part build simulation, which is multi-scale, multi-physics problem in itself and is computationally very expensive. Consequently, support structures are designed today based on experience, and a limited number of physical

experiments. This trial-and-error approach often results in increased production cost. The work presented in this paper introduces the concept of an *aggregate equivalent static load* (ESL) for the design of support structures.

The remainder of this paper is organized as follows. Current strategies for the design of support structures are discussed in Section 2. A truss-type support is proposed in Section 3.1, to illustrate the ESL strategy. Then, the construction of an evolving part-and-support coupled system is presented in Section 3.2. The transient thermal simulation of this coupled system is discussed in Section 3.3. Using the results of transient thermal simulations, aggregate equivalent static loads are defined in Section 3.4, which are used in Section 3.5 to optimize the truss-type support structures. Numerical and experimental results are presented in Section 4 to validate the proposed concepts. Manufacturing considerations are discussed in Section 5. Finally, Section 6 summarizes some of the existing challenges and future work.

2 Literature Review

As mentioned earlier, support structures play a pivotal role in the success of a part build, but they increase the cost of fabrication. Significant progress has been made to reduce or eliminate the need for supports either by (a) changing the part design [13–18], (b) optimizing part build orientation [19–23], (c) optimizing the supports [24, 25] and/or (d) modifying the printing process [26]. However, some of these methods are not applicable to LPBF, while others have not been experimentally verified. In this section, prior work on the design, simulation and optimization of support structures for LPBF have been reviewed.

2.1 Geometry-based Optimization

A plausible strategy to optimize support structures is to use a combination of physical experiments and geometric rules. Calignano [27] varied multiple geometric parameters of block-type supports and carried out physical experiments. Critical parameters were identified based on their signal-to-noise ratio, and supports were then optimized for ease of removal and to minimize warpage. Bobbio et.al [28] tested the strength of block-type supports for anchorage, ease of part removal and post-processing. Zhu et.al [29] proposed tree-type supports; then, several candidate topologies were identified, and optimized using particle swarm optimization to reduce material volume, constrained by parameters that ensured the tree structures were self-supporting. Each optimization took over 2000 iterations to converge, even for a simple cantilever beam, making the approach potentially computationally expensive. Furthermore, the supports were optimized for material volume and not for thermal management. Wang, et.al. [30] identified optimal support points on the overhang surfaces using genetic algorithm. Vaissier et.al [31] used genetic algorithm (GA) to sequentially prune members of a tree-type lattice support. Optimization variables were selected through a design of experiment (DOE) to minimize the support volume. The GA-based optimization reduces support material with constraint on manufacturability, but does not consider heat transfer as an objective. Recently, Zhang, et.al. [32] used GA-based optimization to obtain multiple tree-like supports over a Pareto front. The best support topology with minimum branch tip translations was chosen.

2.2 LPBF Process Simulation

Constructing support structures based on geometric rules can lead to sub-optimal designs. Physics-driven process simulations are essential for constructing optimal designs. Moreover, computer simulation helps in understanding thermal energy distribution and heat dissipation during the LPBF process.

LPBF is a complex multi-scale, multi-physics problem where process parameters, material properties and part geometry play a pivotal role in determining the final part quality [33]. The time and space dependency of thermal energy deposition makes the thermo-mechanical modeling and simulation computationally very expensive [34, 35]. Typically, single-track or single-layer build simulations are performed by solving the heat equation [36–40].

Rosenthal [41] first applied the idea of moving point heat source to obtain heat distribution on a thin metal plate. Analytical solution in 3D for maximum surface temperature have been obtained by Labudovic and Kovacevic [42]. Semi-analytical models have also been proposed to simulate the part build process [43–46], using the concept of moving point heat source. However their assumption of semi-infinite body is not applicable in the presence of support structures.

Zhang, et.al. [47] simulated the temperature field in LPBF using a 3D FEA model with temperature-dependent material properties and a moving Gaussian heat source. A full 3D finite element model also was used by Song, et.al. [48] to better understand the impact of process parameters on part micro-structure properties. Zeng, et.al. [49] investigated the effective thermal properties of support structures in selective laser melting, combining the solidified material and entrapped powders. Liang, et.al. [50] used inherent strain based methods to simulate the deformation of thin-walled block-type supports. Roberts, et.al. [51] proposed the idea of birth and death of element in simulating the 3D transient temperature field in layer-wise laser melting. These numerical approaches in simulating the temperature distribution often use very small specimen sizes owing to the exorbitant computational cost. Also, they neglect the effect of thermal resistance posed by the support structure, which is critical during any actual part built process.

2.3 Physics-based Geometric Optimization

Unlike geometry-based optimization, the strategy here is to use the underlying physics (typically, a simplified thermal simulation) to drive the optimization. Zeng [52] used a combination of material properties, part geometry, initial support structure geometry, scan pattern and process parameters to generate thermal stress profile on a part. The induced thermal stress is then used to compute the maximum support structure parameters for block-type supports. Values obtained from all the layer-wise simulation instances is set as the optimal support structure design. Generating supports with different geometric parameters for every layer simulation can be computationally expensive. Fractal support structures were obtained by optimizing the block-type supports to minimize residual stresses by Krol et.al [53].

2.4 Topology Optimization for AM

Topology optimization (TO) has also been used for minimizing support structures for AM. There are two different themes in this context.

1. Optimize part for minimum support: Here the focus is on avoiding overhang surfaces to ensure self-supporting parts. Zhao et.al [54] added overhang angle constraint in TO formulation so that the edges on a part are aligned towards build direction for self-support. Van et.al [55] added accessibility filter in TO to ensure overhang surfaces are generated only if the supports are accessible. Gaynor and Guest used overhang and minimum length scale constraints to generate topologies with no support requirement. Langelaar [56] analyzed the trade-off between adding strict no-overhang constraints and having supports on topology optimized designs manufactured for AM. In all of these cited works, only numerical results were presented with no discussion on the manufacturability of the parts. Similarly, Leary et.al [13] modified the optimized topology of parts to avoid internal and external overhang boundaries. Qian [57] added Heaviside projection based integral as constraints to control the slopes of boundaries for self-support. Mirzendehdel and Suresh [16] added constraints on the support structure volume to optimize the topology of parts, using the idea of topological sensitivity of supports. The results for fused deposition modeling (FDM) based AM were presented. These methodologies might not be applicable to LPBF since the physical processes differ significantly.

2. Optimize part and support structures: Here the focus is on generating optimal support structures using TO. Mezzadri [24] generated self-supporting support structures using topology optimization with uniform structural loading. Allaire and Bogosel [58] proposed multiphase optimization involving simultaneous optimization of part as well as supports, subjected to overhang constraints and constant heat flux loads. Once again, these techniques target FDM rather than LPBF. Amir and Amir [59] used solid-void and void-lattice-solid parametrization to optimize the topology of part and supports. Objective function consists of a sum of weighted compliance due to body forces obtained from intermediate stages of layer-wise build. Zhou et.al [60] used topology optimization for part design as well as supports by identifying areas of high temperature due to transient heat loading on 2D geometries. Pellens et.al [61] used inherent strain method to investigate thermal deformations during LPBF process. The TO framework generates support structures to limit the vertical structural deformations. Wang and Qian [62] generated optimal part and support structures through TO using constant heat flux on the overhang surfaces. Paggi et.al [63] proposed the use of topology optimization to reduce the material usage; however, no experimental results were presented. Kuo et.al [64] used multi-objective TO to generate support structures that are easy to remove and minimize cost. A twig-like support structure was generated under compliance constraint to minimize part deformation with minimum support material, and time to print and removal. Zhou et.al [60] used the temperature deviation with respect to the ambient, from a layer-wise transient simulation, as the objective for topology optimization. Overhang constraints were added along with an AM filter for self-support. However, the results were not validated through physical experiments. Bartsch et.al [6] proposed support structures optimized for heat dissipation. Layer-wise thermal simulation of part build was carried out using element birth-death method to obtain maximum temperature distribution, occurring over the first overhang layer. A design domain was then determined using the overhang points,

which underwent thermal topology optimization to generate supports. Numerical results demonstrated the effectiveness of the method, however no physical experiments were presented to validate the idea. The use of the heat load from just the first overhang layer simplifies the design process, but was not justified. Recently, Lee and Yun [65] used transient analysis for lattice structure topology optimization. Effective part-scale thermal load is obtained from the transient thermal simulations with flash heating of each layer. Results from manufacturing of parts using the lattice type supports are presented. Similarly, Cheng et.al [66] generated graded lattice supports using topology optimization. These optimized structures prevent stress-induced cracking due to residual-stresses. However, they incur higher post-processing costs due to large contact area. Huang et.al [67] used TO to generate lattice type support structures and compared their role in warpage against conventional support structures. Manufactured results for cantilever beam showed lattice supports with lower warpage deformation with better thermal management, than the other supports. However, the test specimens do not involve evolving topologies, which change the thermal distribution at each layer built process in LPBF. Miki and Nishiwak [68] simulated the layerwise build process of LPBF and obtained aggregated thermal loads from entire build of parts, which are then used in generating topology optimized supports for all the overhang surfaces. The stiffness of supports and the added heat transfer paths due to supports during the part build have not been considered in generating the supports.

Although TO provides promising results, their applications in LPBF still requires further attention, specifically in terms of manufacturability. One can identify the following research gaps on the use of TO in generating optimal supports.

- Previous studies primarily focus on numerics and the competence of numerical results is not often demonstrated through experimentation. Manufacturability of parts and supports in LBPF are critical for validation of the proposed ideas.
- Most of the results for manufacturing are targeted towards FDM, and not LPBF.
- Topology optimized designs do not always lead to AM friendly designs [16] and require geometric post-processing for downstream applications [69].
- Evolving part and support geometry dictate the need for transient thermal analysis, and this is often neglected.

2.5 Paper Contributions

To address these shortcomings, we propose a novel aggregate equivalent static load (AESL) based optimization. Transient thermal simulation of layer-wise part built process, with an evolving support, is carried out using equivalent-layer heating [70–72]. The transient thermal loads are converted to an equivalent static load, followed by an aggregation to account for the cumulative build process. The concept is demonstrated using a truss-type support, where the cross-sectional areas of truss members are optimized using the methods of moving asymptotes. Finally, these optimized truss-type supports are converted to a finned design, that have adequate structural strength, and are easy to remove. This is then validated through manufacturing of specimens with varying size, shapes and complexities.

3 Proposed Strategy

In this paper, simplified transient thermal simulations are carried out to generate optimal supports using the proposed concept of equivalent static thermal load (ESL). In particular, the idea of ESL is demonstrated using a truss-type support structure. The proposed workflow is presented in Figure 2, and discussed below. For a given part, the overhang surfaces are identified. A new greedy algorithm is proposed to construct tree-like support for these overhang surfaces. Based on a user-defined support volume, uniform cross-sectional areas are initially assigned to all support members. The part and support are then coupled to carry out a transient thermal simulation. The transient results are then converted to equivalent static load (ESL) at the end of each mesh layer. An aggregate of these equivalent static loads is obtained at the end of simulation. The aggregate ESL is finally used to optimize the cross-sectional areas of the support structures.

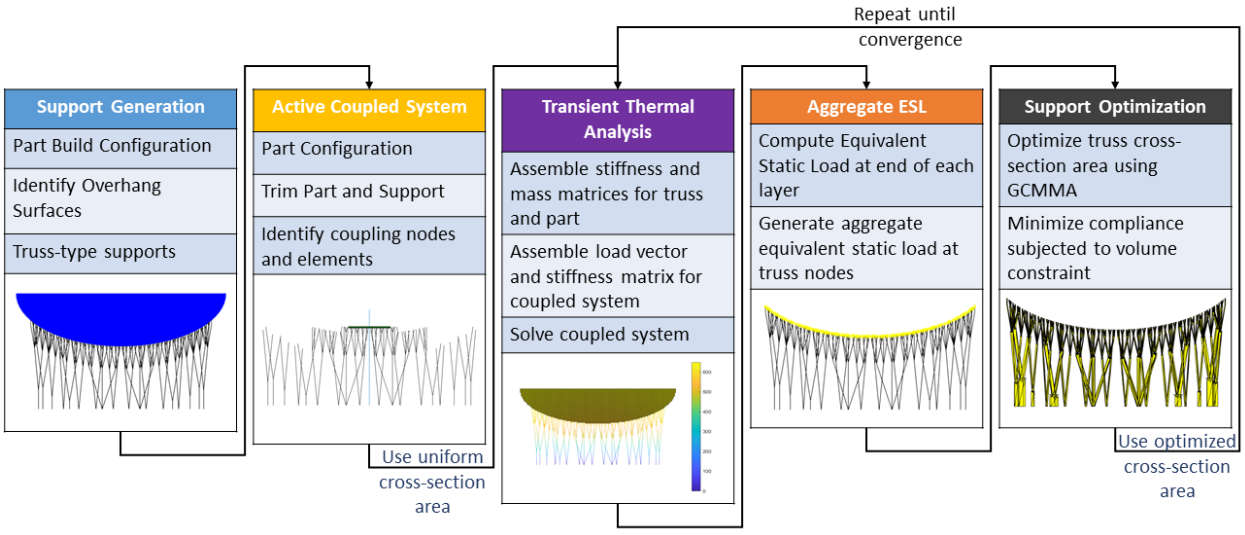

Figure 2: *Proposed strategy to optimize support structure for LPBF.*

3.1 Truss-type Supports

A truss-type support is considered here to illustrate the proposed ESL strategy. A tree-like support structure is generated using a greedy algorithm based on the need for support at any overhang point on a part. Similar support structures have been used in fused deposition modeling (FDM). For example, Vanek et.al [73] generated tree-like topologies through the intersection of support cones. Zhou et.al [74] used Lindenmayer system (L-system) and octree to generate tree-like supports. Lantada et.al [75] used bio-inspired fractal tree-like supports for Stereolithography (SLA). Weber et.al [76] studied the effect of different geometric parameters on the printability of parts using tree-type supports for LPBF. Cause-effect-relations matrices for process parameters with the part/support build properties were presented. The results could be used for generating better support structures. Zhu et.al [29] have proposed an algorithm to generate tree topology for supports for LPBF. Each branch node on a tree is allowed to connect to a maximum of 6 nodes from the overhang surface. The supports are then optimized to minimize volume by a greedy particle swarm optimization algorithm.

Vassier [31] used a genetic algorithm to remove lattice members, ultimately creating a tree-like structure for LPBF. Theoretically, these supports could potentially use less material than those generated using commercial software. However, most of these tree-type supports require manual interactions.

Here, a novel greedy algorithm for generating truss-supports is proposed. The 2D version of the algorithm is illustrated in Figure 3 and described below. It is assumed that a part is represented by a collection of surface triangles, and saved as an .STL file.

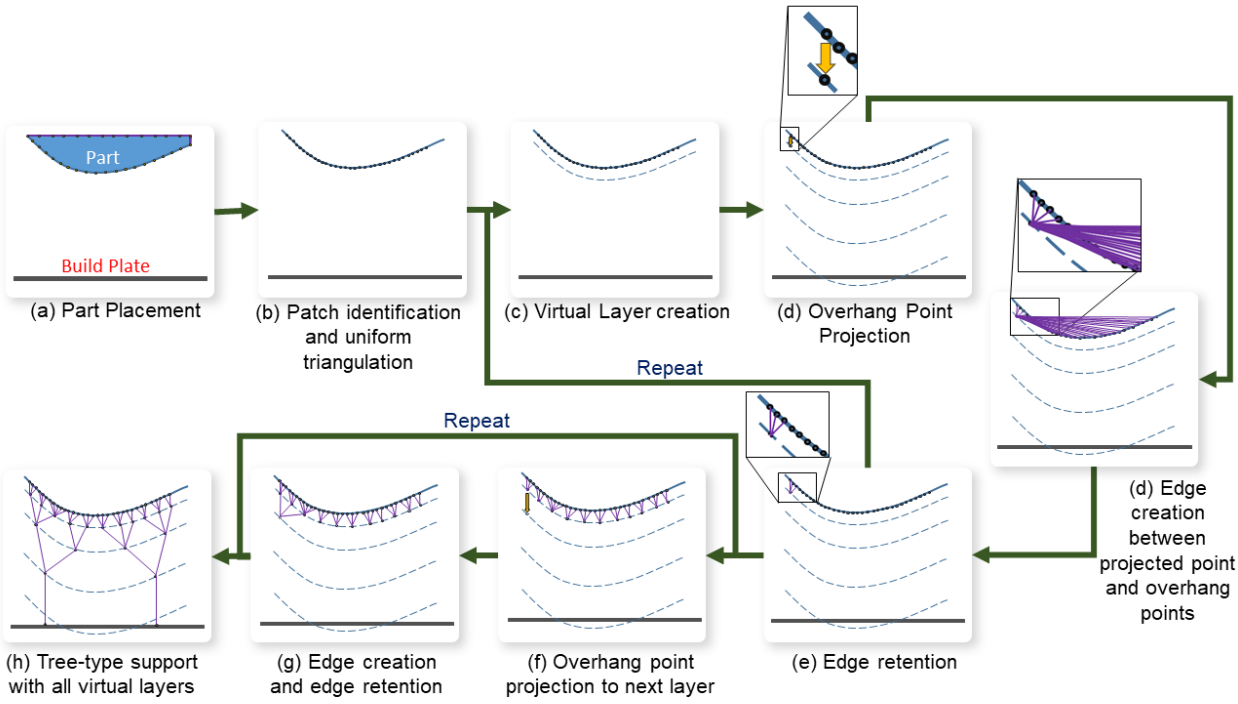

Figure 3: *Algorithm for truss support generation.*

(a) Once a build-direction is chosen (see [19, 20, 77]), the part is placed over a build plate at a desired build height. A minimum of 5 mm build height is recommended to ensure sufficient clearance for part removal.

(b) The triangles representing the overhanging surface of the part are extracted based on their surface normal inclination (usually 45°or less) with the build direction. These surface triangles form an *overhang surface patch*, which are then re-triangulated to generate triangles with edge length equal to *inter-comb distance*. The latter is a machine dependent parameter and is usually specified by the manufacturer. These support points play a pivotal role in print quality as well as post-processing costs [30]. A recommended value of 0.6mm [78] is used here to ensure adequate support of overhang surfaces.

(c) Then, a virtual layer is created by offsetting the overhang surfaces patch by a distance larger than the inter-comb distance to ensure self-supporting edges.

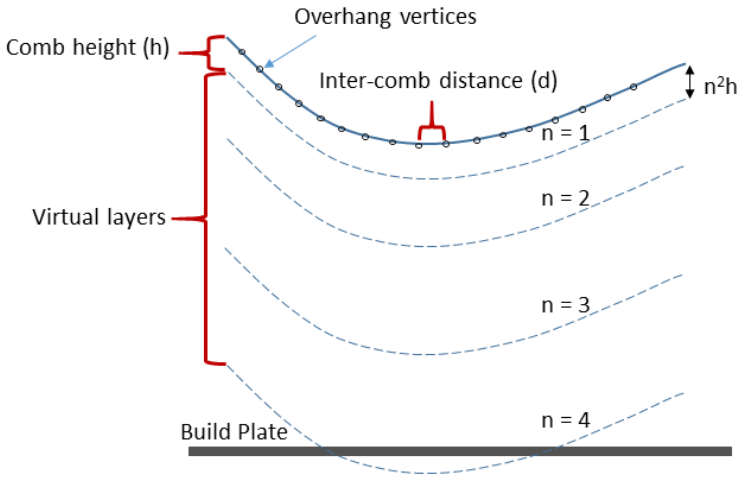

Figure 4: *Virtual layer and associated parameters.*

(d) The first vertex on the re-triangulated patch is then projected onto the first virtual layer. The remaining overhang points are then connected to this projected point. The inclination of connecting lines are compared against the threshold support angle. A threshold support angle is the maximum allowable angle of inclination of lines with the build direction that ensures self-support. Note that a lower value of support angle (30°to 35°) reduces the number of edges, thereby preventing points of heat concentration as well as provides better distribution of supports, as illustrated in Figure 5.

(e) The connecting lines that conform to the angular inclination constraint are retained. All projected points are moved to the center of corresponding supported points. The next unsupported overhang vertex on the patch is then projected to the first virtual layer, and the process is repeated until all overhanging points are supported.

(a) *Truss with large threshold angle (50°)* (b) *Truss with small threshold angle (35°)*

Figure 5: *Role of threshold angle in generating tree-type support*

(f) Once all overhanging points are supported, a new virtual layer is created. Successive virtual layers are spaced at increasing distance as illustrated in Figure 4, to limit the number of vertical beams (since vertical beams can lead to recoater collision). Points from the first layer are projected onto the second virtual layer.

(g) The process of edge creation is repeated until all projected points are supported.

(h) The algorithm is repeated and terminates when a virtual layer reaches the build plate. Thus, all the projected points are either supported, or in contact with the build plate.

Some of the salient features of the proposed algorithm are

- The tree topology is not structured, leading to a larger design space for optimization.
- The parameters of the algorithm can be customized for a specific LPBF manufacturer.
- Due to the nature of the tree construction, disconnected and overhang edges are avoided.
- Virtual layers allow for automatic and gradual convergence of edges from the overhang surface to the build plate.
- The algorithm does not limit the number of edges meeting at a point on successive virtual layers, rather it is defined by the minimum threshold support angle to ensure self-support.
- The commonly used *Block-type* supports entrap powder and are not easy to optimize for heat transfer or material usage. The proposed truss-type supports are easier to optimize, do not entrap powder, and are easier to remove.

Existing geometric algorithms generate optimized support truss topology where the objective is to minimize the total length of the truss members. The proposed tree algorithm generates support for every overhang node, while the optimization is performed on the cross-section areas for better heat transfer. Thus, the two approaches are not directly comparable for time complexity. The truss-type supports here are generated within a couple of minutes for complex geometries.

3.2 Active Coupled System

An evolving active system comprising of supports and part layers is used to simulate the layer-wise build. A part is first meshed using hexagonal elements (voxels). The size of a voxel affects the computational time and accuracy of results [79], and is determined by the minimum feature size of the part, and the resolution of printer [80, 81]. In this study, the voxel size is chosen to be 20 times the powder layer thickness. Mesh convergence studies are also performed to understand the effect of voxel size on the simulation results. Once the part is meshed, the mesh can be trimmed to simulate layer-wise build. Similarly, the truss-type support can also be trimmed; a typical trimmed active system is illustrated in Figure 6. To enforce connectivity between the part and support, for every hanging truss node, the corresponding hex element is identified based on proximity as illustrated in Figure 6. The truss node and corresponding hex-element nodes will be coupled as described below.

3.3 Transient Thermal Simulation

A transient thermal finite element formulation to solve the active coupled system is discussed next. Convective and radiative heat dissipation are usually neglected [51, 82–84]. Furthermore, heat absorption and latent heat effect are also neglected here as the problem

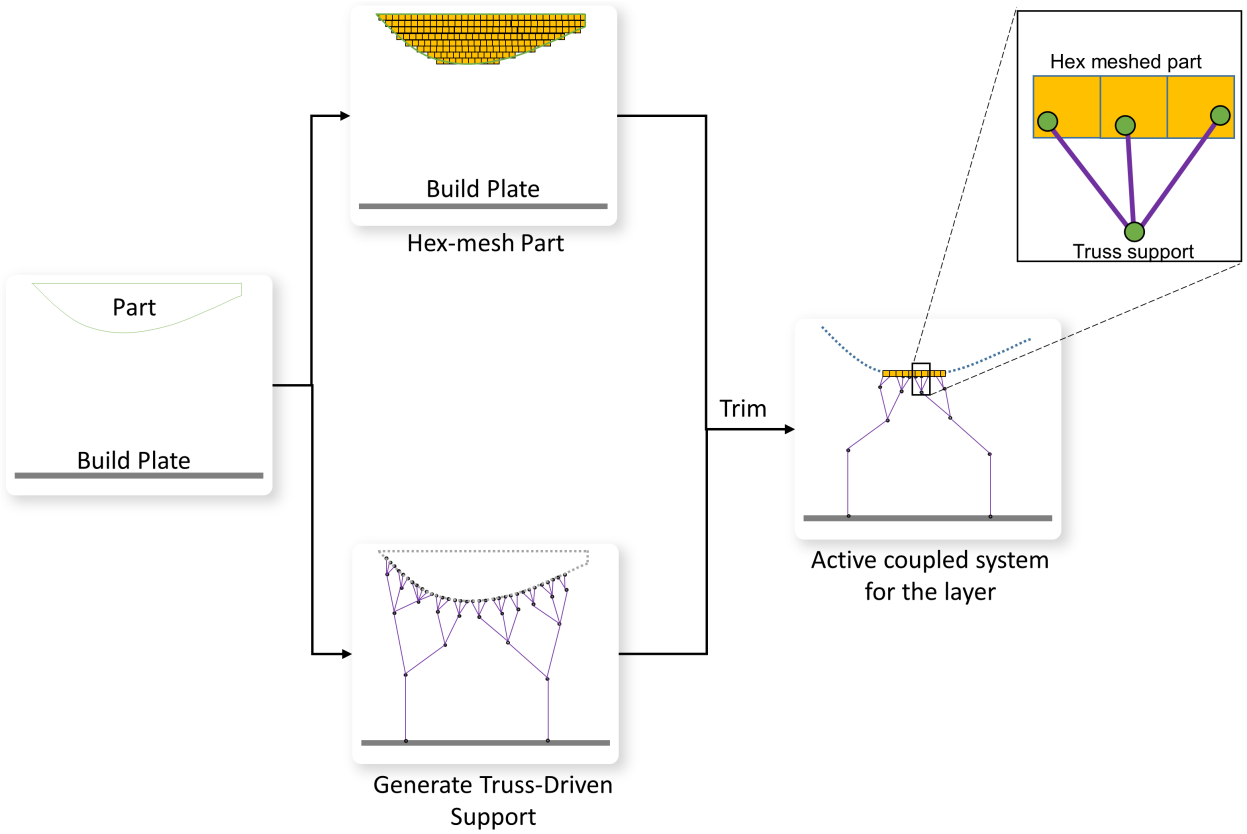

Figure 6: *Evolving coupled system.*

is solved at a macroscale (layer-wise) rather than at a microscale (melt-pool size). Owing to the negligible thermal conductivity of the metal powder bed [1, 2], conductive heat transfer through metal powders is also neglected. Finally, material properties (specific heat capacity, thermal conductivity and density) are referenced at room temperature, and are assumed to be constant for simplicity.

Transient thermal FEA is solved at a mesh-layer scale (macro-scale) [85, 86]. A single mesh layer, often called a meta-layer [87, 88], is composed of a number of physical powder layers. For this work, each meta-layer is chosen to represent 20 powder layers. Meta layer thickness of 750μm to 1mm have previously been used [71,86]. The assumption of meta-layer thickness of 20 layers (400μm) is a balance between speed and accuracy.

The entire meta-layer is subject to equivalent-layer heating [70–72], to avoid computationally expensive laser scanning strategies as this work primarily targets global support structure optimization.

First, elemental stiffness matrices (k_{truss}, k_{hex}) and elemental mass matrices (m_{truss},m_{hex}),

for both 1D-truss elements and 3D-hex elements, are computed as follows:

$$\begin{aligned}
\left[k_{truss}\right] &= \frac{\alpha A_e}{l_e}\begin{bmatrix} 1 & -1 \\ -1 & 1 \end{bmatrix} \\
\left[k_{hex}\right] &= \int_{\Omega_e} [\nabla N_{hex}]^T [D_{hex}][\nabla N_{hex}]\, d\Omega_e \\
\left[m_{truss}\right] &= \frac{\rho c_p A_e l_e}{6}\begin{bmatrix} 2 & 1 \\ 1 & 2 \end{bmatrix} \\
\left[m_{hex}\right] &= \int_{\Omega_e} \rho c_p [N_{hex}]^T [N_{hex}]\, d\Omega_e
\end{aligned} \tag{1}$$

where, N_{hex} are the finite element shape functions for the hex elements, ρ is the density, c_p is the specific heat capacity, α is the thermal conductivity, A_e and l_e are the area and length of the truss element, and D_{hex} is the 3D elasticity matrix. Then, the two global thermal stiffness matrices, K_{hex} and K_{truss}, and the thermal mass matrices M_{hex} and M_{truss} are assembled. For coupling, a constraint matrix C is constructed where the entries of C are computed using the contributions of 3D hex-shape functions at the corresponding truss point (see Figure 6).

These matrices are finally assembled as follows:

$$K_{coupled} = \begin{bmatrix} K_{hex} & 0 & \\ 0 & K_{truss} & C^T \\ & C & 0 \end{bmatrix}, M_{coupled} = \begin{bmatrix} M_{hex} & 0 & \\ 0 & M_{truss} & C^T \\ & C & 0 \end{bmatrix} \tag{2}$$

The thermal load F^i on each of the nodes on the top layer of hex-elements is computed using volumetric energy density (VED) [89, 90]:

$$VED = a\frac{P}{v h_t h_s} \tag{3}$$

$$F^i = \frac{VED}{N t_{ls}} V_L \tag{4}$$

$$t_{ls} = \frac{N_h A_h}{h_s v} \tag{5}$$

where a is the laser absorptivity of metal powder, P is the laser power, v is the laser scan speed, h_t is the metal powder layer height, h_s is the hatch spacing during laser scan, V_L is the volume of material deposited at the layer L, and N is the number of nodes on the top layer, t_{ls} is the layer scan time computed using the exposed surface area, laser hatch speed and speed; this was motivated by similar models used in [87,91]. The reason for this simple choice is that precise transient temperature is not critical for optimization. Instead, through optimization, the goal is to achieve a relative reduction in thermal compliance.

To solve for transient temperatures on the coupled system, Neumann boundary conditions are applied to the top layer of hexagonal elements with heat flux(F^i) computed in Equation 4, while the truss nodes in contact with build plate are assigned a Dirichlet boundary condition with fixed chamber temperature.

The transient problem is then solved using Newmark-Beta [92, 93] scheme, with $\beta = 1$, is chosen for time-stepping. This leads to:

$$[K_{eff}]\{T_{n+1}\} = \{F_{eff}\}_{n+1} \tag{6}$$

where, K_{eff} and F_{eff} are the effective global stiffness matrix and force vectors given by,

$$[K_{eff}] = \frac{1}{\Delta t}[M_{coupled}] + [K_{coupled}] \tag{7}$$

$$\{F_{eff}\}_{n+1} = \frac{[M_{coupled}]}{\Delta t}\{T_n\} + \{F\}_{n+1} \tag{8}$$

and

$$T = \begin{bmatrix} T_{hex} \\ T_{truss} \\ \lambda \end{bmatrix} \tag{9}$$

where λ's are the Lagrange multipliers.

Equation 6 must be solved twice, once at the end of laser scan, and another for recoater travel. For the first simulation, the time step $\Delta t = t_{ls}$ and F is the applied thermal load, whereas, for the second simulation, $\Delta t = t_{rt}$ and $F = 0$ are used. t_{rt} is the time for recoater travel to lay a new layer of powder. The second FEA incorporates the effect of conductive heat dissipation during recoater travel for each of the meta-layers.

The transient solution for the truss is now used to construct equivalent static loads (ESL). Equivalent static load (ESL) due to equivalent-layer heating [70–72] heating of each layer is computed after the first FEA. ESL has been used extensively in dynamic structural optimization [94–100]. For example, Dattakumar [95] used modal transient analysis along with a scaling factor to obtain ESL, while Yi et.al [101] used stress correction factor along with the equivalent static loads to approximate the non-linear stress response in crashworthiness. Zhang et.al [99] used dominant vibration modes to determine ESL for seismic structures. Jang and Lee [100] computed multiple ESLs for dynamic response topology optimization and then the structures were optimized to minimize response near the dangerous time steps. However, in all these scenarios, the structural domain does not change during the transient analysis. In LPBF, both the domain as well as the thermal loads evolve with time.

As this work is intended towards designing optimal truss support, the equivalent static load (ESL) for the truss, at the end of each layer (L), is defined as follows:

$$\{f^L_{ESL}\} = [K^L_{truss}]\{T^L_{truss}\} \tag{10}$$

3.4 Aggregate Equivalent Static Load

This section discusses how the equivalent static load computed from the transient solution is further used to find the maximum loading on the truss during the entire part build process. An aggregated approach for ESL is required in order to account for the evolving domain and the transient nature of load.For every node j of the truss, the aggregate equivalent static load $f_{AESL}(j)$ at node j is defined as the maximum equivalent static load $f^L_{ESL}(j)$ over all layers L, i.e.,

$$f_{AESL}(j) = \max(f^L_{ESL}(j)) \qquad\qquad L = 1, 2, .., L_{max} \tag{11}$$

In summary, the algorithm for layer-wise transient simulation of coupled active system is presented below.

Algorithm 1 Transient Thermal Analysis for Coupled Active System

Initial Temp = Chamber Temp
for $L = 1$ to maxLayer **do**
    Compute active truss and hex-mesh
    Compute K_{hex}, M_{hex} and K_{truss}, M_{truss}
    Assemble $K_{coupled}$ and $M_{coupled}$ matrices
    Compute F
    Compute K_{eff} and F_{eff} for laser scan
    Solve for T^L_{n+1} at the end of laser scan
    Compute f^L_{ESL}
    Initial Temp = T^L_{n+1}
    Compute K_{eff} and F_{eff} for recoater travel with $F = 0$
    Solve for T_{n+1} at the end of recoater travel.
    Initial Temp = T_{n+1}
end for

3.5 Support Structure Optimization

Truss-type support optimization is optimized using the aggregate ESL. This is carried out by minimizing thermal compliance of the truss system subjected to a volume constraint, i.e.,

$$\begin{aligned} \min_{\{A_i\}} \quad & J = \{f^T_{AESL}\}\{T_{truss}\} \\ \text{s.t.} \quad & [K_{truss}]\{T_{truss}\} = \{f_{AESL}\} \\ & h = \sum_{e=1}^{m} \frac{A_e l_e}{V^*} - 1 \leq 0 \\ & A_e^{min} \leq A_e \leq A_e^{max} \end{aligned} \tag{12}$$

where, J is the thermal compliance, f_{AESL} is the aggregate equivalent static load, K_{truss} is the global truss stiffness matrix, T_{truss} is the truss nodal temperatures (an unknown in this optimization problem), A_i's and l_i's are the cross-sectional areas and lengths of the truss members, m is the total number of truss elements, and V^* is the allowable support structure volume. The truss topology remains unchanged throughout the optimization; therefore there is no change in the length (l_i) or orientation of the truss members. The minimum bound for the areas is set to the printer resolution to ensure manufacturability, while the maximum bound is set 10 times the initial area. The compliance minimization problem is self-adjoint, so it does not involve solving an additional adjoint problem during optimization. For optimization, the globally convergent method of moving asymptotes (GCMMA) [102] is utilized. The optimization runs converged in 150 to 200 FEA iterations. Furthermore, since the optimization only involves truss system, it is computationally inexpensive.

3.5.1 Sensitivity Computation

The GCMMA optimizer requires an objective function, constraints, sensitivity of objective function and the sensitivity of constraints. The sensitivity of the objective function

(thermal compliance) with respect to the design variables (i.e., truss cross-section areas) is computed as follows.

$$\frac{\partial J}{\partial A_e} = \{f_{AESL}^T\}\frac{\partial\{T_{truss}\}}{\partial A_e} \tag{13}$$

i.e.,

$$\frac{\partial J}{\partial A_e} = ([K_{truss}]\{T_{truss}\})^T\frac{\partial\{T_{truss}\}}{\partial A_e} \tag{14}$$

Differentiating the state equation, we have

$$\frac{\partial[K_{truss}]}{\partial A_e}\{T_{truss}\} + [K_{truss}]\frac{\partial\{T_{truss}\}}{\partial A_e} = 0 \tag{15}$$

i.e.,

$$[K_{truss}]\frac{\partial\{T_{truss}\}}{\partial A_e} = -\frac{\partial[K_{truss}]}{\partial A_e}\{T_{truss}\} \tag{16}$$

From Equation 16 and Equation 14, we get

$$\begin{aligned}\frac{\partial J}{\partial A_e} &= -\{T_{truss}^T\}\frac{\partial[K_{truss}]}{\partial A_e}\{T_{truss}\}\\ \frac{\partial J}{\partial A_e} &= -T_e^T\begin{bmatrix}1 & -1\\ -1 & 1\end{bmatrix}T_e\frac{\alpha_e}{l_e}\end{aligned} \tag{17}$$

where, T_e is the temperature, l_e is the length and α_e is the thermal conductivity of truss element e. Similarly, the sensitivity of constraints is given by

$$\frac{\partial h}{\partial A_e} = \frac{l_e}{V*} \tag{18}$$

The objective function and constraints are scaled for numerical robustness.

3.6 Cross-sectional Design

Once the cross-sectional areas are optimized, it can be used to generate appropriate cross-sectional geometry. Consider Figures 7a - 7e where various fin cross-sections and a circular cross-section are illustrated. The thickness of the fin-designs is determined by the meltpool thickness for a single laser pass, which is typically between 120μm to 160μm, for EOS M290. To choose between these cross-sections, various factors including file size, build time, post-processing effort, buckling strength and thermal characteristics must be considered.

The fin designs require fewer triangles for representation, i.e., lead to a smaller file size than the circular designs. Furthermore, they are easier to fabricate since each fin requires a single laser pass. Finally, they exhibit better buckling strength due to their larger bending moment of inertia. This is illustrated in Figure 7f where one can observe, for example, that, for the same cross-sectional area, the 4-fin design exhibits five times the buckling strength of the circular design. However, the fin designs exhibit poor overlap at the joints, reducing the effective area for heat transfer. This can lead to burning/oxidation and part warpage. In comparison, the circular designs exhibit good heat transfer at the joints, but are poor otherwise, i.e., have poor buckling strength, lead to large file-size, etc.

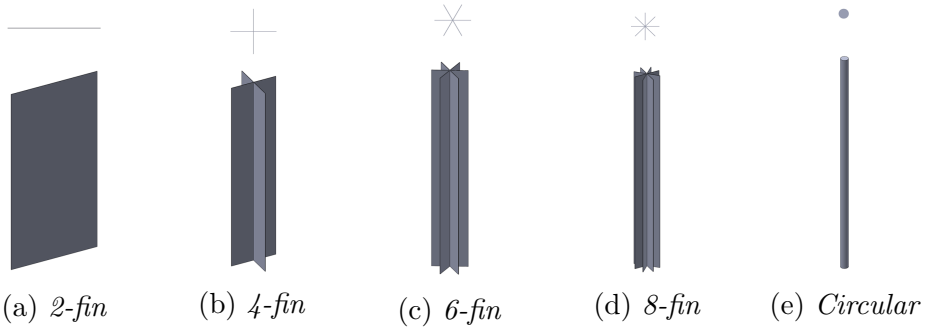

(a) *2-fin* (b) *4-fin* (c) *6-fin* (d) *8-fin* (e) *Circular*

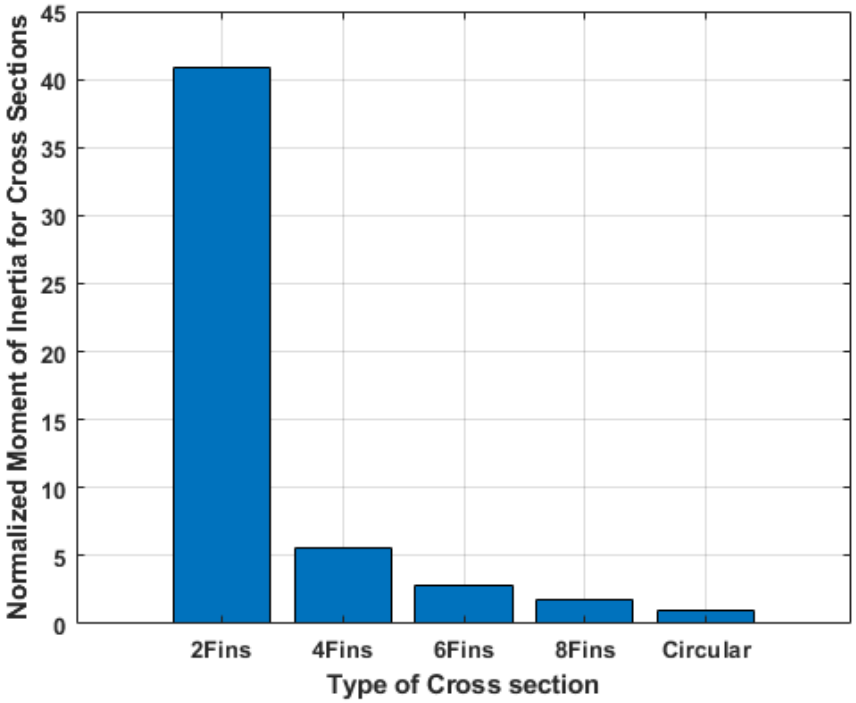

(f) *Relative buckling strength.*

Figure 7: *Cross-section for truss members and their relative buckling strength.*

The above observations were confirmed through a simple experiment. A rectangular plate was printed with a four-fin design, and a circular design for the supports; see Figure 8a and Figure 8b. As one can observe in Figure 8a, the fin design exhibits significant burning/oxidation at the nodes and consequently breakage.The four-finned designs led to disruption in heat transfer due to insufficient overlap at joints as can be observed in Figure 9a, i.e., there is a significant reduction in effective area for heat transfer. We hypothesize that this was the root cause of burning. On the other hand, the circular design exhibits good thermal characteristics, but buckled. Buckling of similar truss-type support members with circular cross-section was also observed in Weber [76]. We hypothesize that the warping of the outside edges results in compressive forces on the truss members in the middle, leading to buckling.

Based on the analysis and experimental results, a hybrid cross-section truss member is

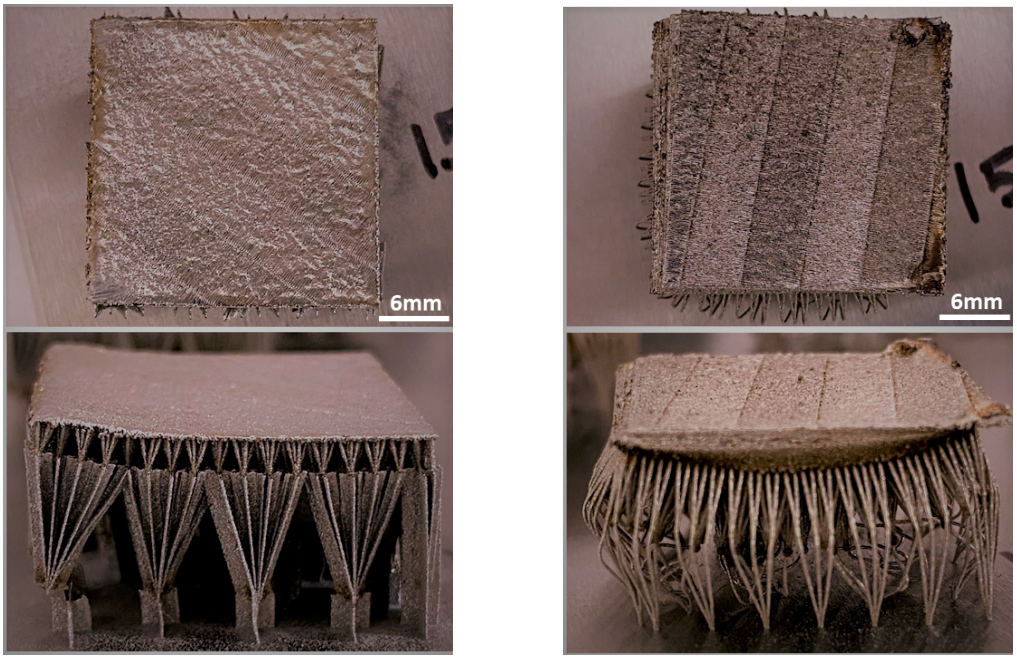

(a) *Finned Design* (b) *Circular Design*

Figure 8: *Failed specimens with pure fin and pure cylinder cross-sections.*

proposed as illustrated in Figure 9b. The ends are octagonal (to reduce the file size for printing and to improve heat transfer), while the remainder of the truss is four-finned to improve buckling strength. A comparison of buckling resistance of the hybrid design with 4-finned and hexagonal design is shown in Figure 10. The buckling resistance versus aspect ratio (length/area) plot for the truss members with different designs indicate that the hybrid design has comparable strength as that of the four-finned design.

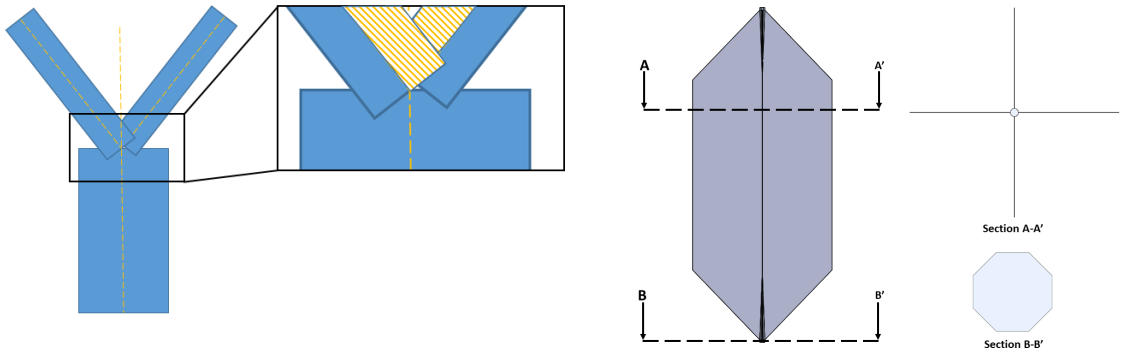

(a) *Issues with finned design.* (b) *Hybrid cross-section.*

Figure 9: *Cross-section design for truss-type supports.*

4 Numerical Experiments

Several numerical experiments were carried out to test the efficacy of the proposed framework. Two different specimens were chosen for the experiments. The hemisphere is a simple

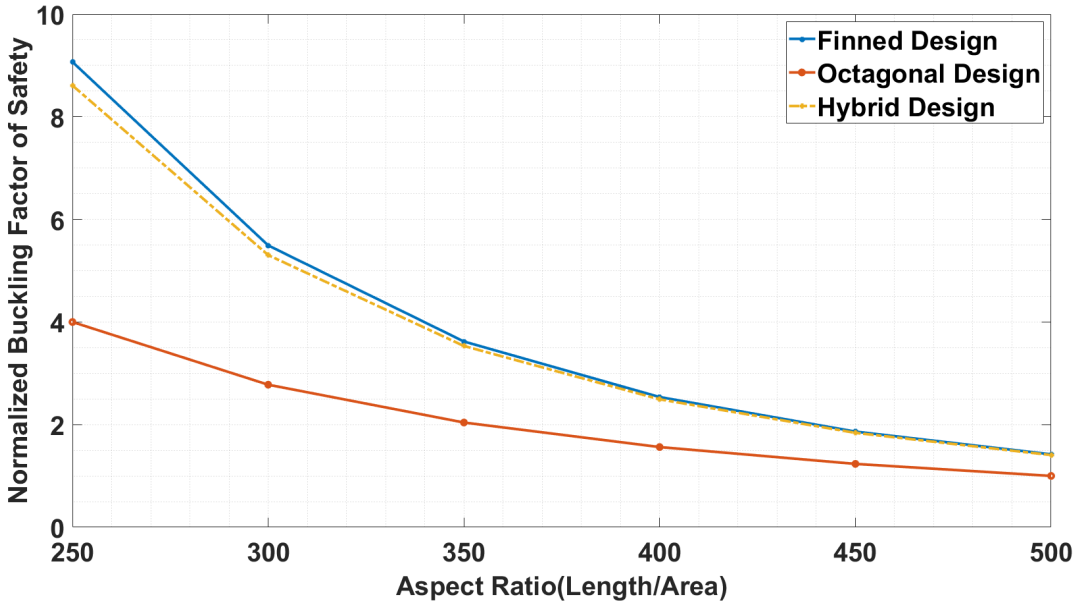

Figure 10: *Buckling Resistance for Different Truss-Member Designs.*

part in Figure 11a that requires a continuously varying support, whereas the support for the clevis in Figure 11b, dimensions in mm, is at a fixed height. However, the clevis exhibits small features and multiple islands, and it is used here to illustrate the generality of the truss-generating algorithm.

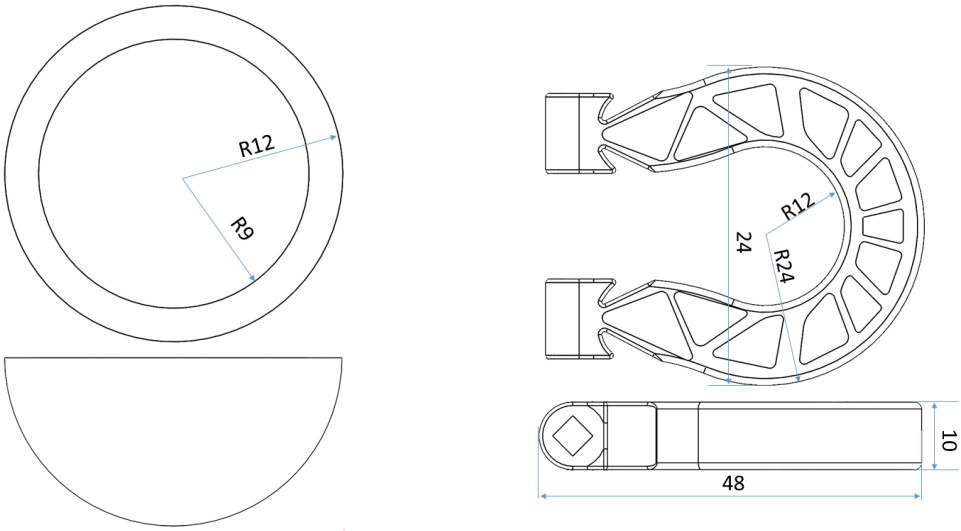

(a) *Hemisphere* (b) *Clevis*

Figure 11: *Specimens used for numerical and physical validation.*

Geometric parameters governing the truss-type support topology are listed in Table 1. The part built simulation, discussed earlier, only considers thermal energy required to melt the powder for building a part, while neglecting the energy input and other process parameters for the thin truss-type supports. The laser scan parameters (hatch spacing, scan pattern)

have also been neglected, considering the equivalent-layer heating-based transient thermal loading during FEA. These dependent parameters for transient thermal simulation of part build, are listed in Table 2 for Stainless Steel (SS316L) metal powder with room-temperature material properties given in Table 3.

Truss Parameters	**Value**	**Units**
Inter-comb distance	0.6	mm
Part Clearance Height	5	mm
Comb Height	0.9	mm
Threshold support angle	50	degrees
Support angle for truss	35	degrees

Table 1: *Support Design Parameters.*

Process Parameters	**Value**	**Units**
Melt Pool thickness	120	μm
Powder Layer Height	20	μm
Laser Absorptivity	0.6	
Laser Scan Speed	1083	mm/s
Laser Power	195	W
Laser Focus Diameter	100	μm
Hatch Spacing	90	μm
Chamber Temperature	80	°C
Recoater Travel Time	10	s

Table 2: *LPBF Process Simulation Parameters.*

Parameter	**Values**	**Units**
Thermal Conductivity	13.8	W/mK
Heat Capacity	450	J/K
Density	8000	kg/m^3

Table 3: *Material Parameters [103, 104].*

While the numerical experiments and physical validation were carried out for both specimens, detailed numerical results are presented below only for the hemisphere since clevis led

to identical conclusions. Unless otherwise mentioned, for the hemisphere: (1) The support volume is 16.4% of the total volume underneath its overhang surface. (2) Uniform cross-sectional areas are initially assigned for all truss members based on this support volume. (3) The part is discretized using hexahedral elements as shown in Figure 12 such that every mesh layer corresponds to 20 powder layers.

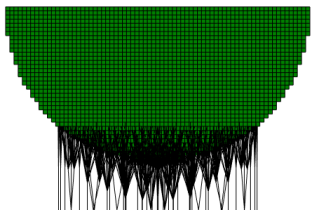

Figure 12: *Discretized hemisphere with support.*

4.1 Transient Temperature

With 16.4% support volume fraction, and uniform area assigned to truss members, Figure 13 illustrates the maximum temperature over the entire active truss-type support, as a function of time, obtained from the equivalent-layer heating. The spatial location of this maximum temperature changes over the simulation period. The temperatures are overestimated due to various simplifying assumptions in the proposed model. The actual temperatures are however not critical for the targeted objective of optimizing the support structures. The band-saw tooth pattern in Figure 13 captures the heating and cooling cycles during layer-wise part build, and the vertical line indicates the instance when the overhang surface ends.

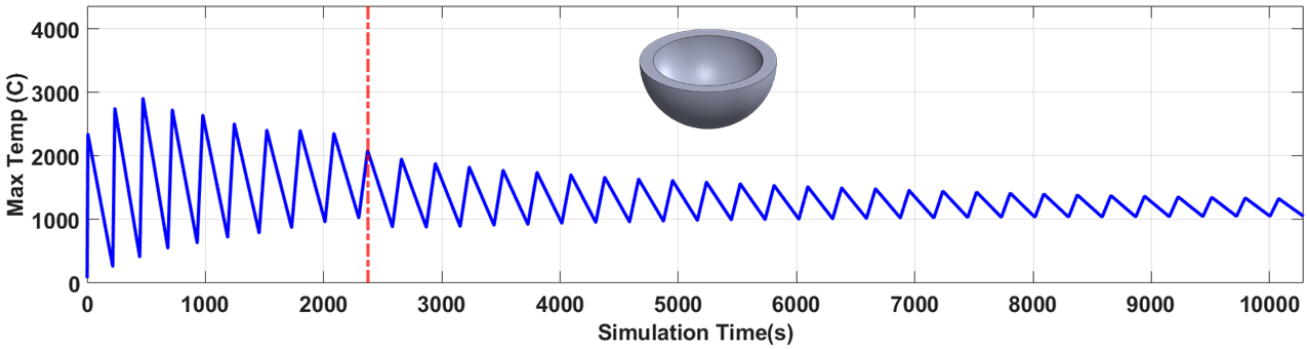

Figure 13: *Temperature cycle for the hemisphere.*

4.2 Mesh Convergence

The impact of mesh density on the simulation results was investigated. Three different meshes with varying hex mesh-element height were chosen for this experiment. The maximum temperature variation per layer as a function of simulation times is plotted in Figure 14. The truss-support topology remains fixed, and for all the cases, uniform cross-section area

was assigned. For three different ratios of hex mesh-element height to physical metal powder height of $20\mu m$, the variation in maximum temperature was observed to be relatively small. As this ratio is increased, the number of temperature cycles decreases as expected, leading to a shift in the saw tooth pattern.

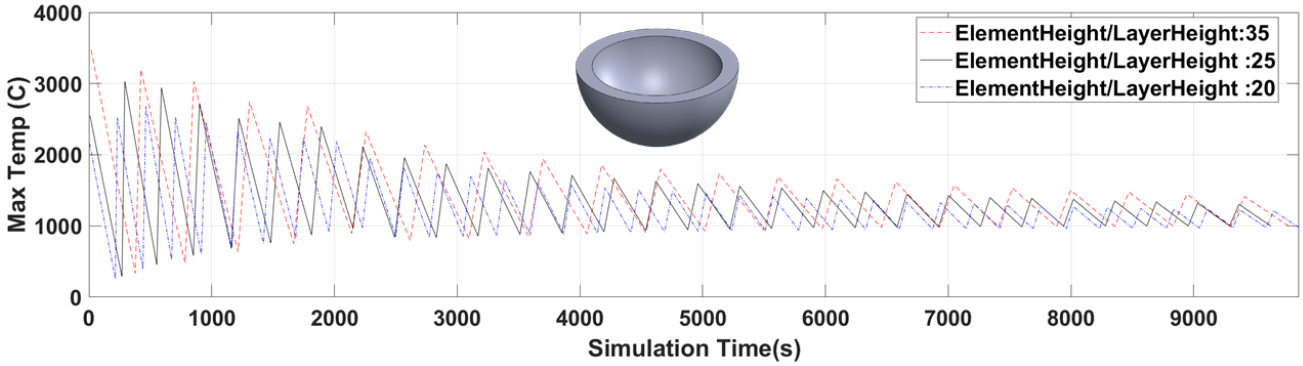

Figure 14: *Mesh convergence study for the hemisphere.*

4.3 Optimization

Finally, the truss-type supports were optimized for minimizing thermal compliance subjected to support volume constraint. For hemisphere subjected to support volume fraction constraint of 16.4%, a reduction of 77% in thermal compliance was achieved. The effect of maximum temperature variation due to optimization is illustrated in Figure 15. The opti-

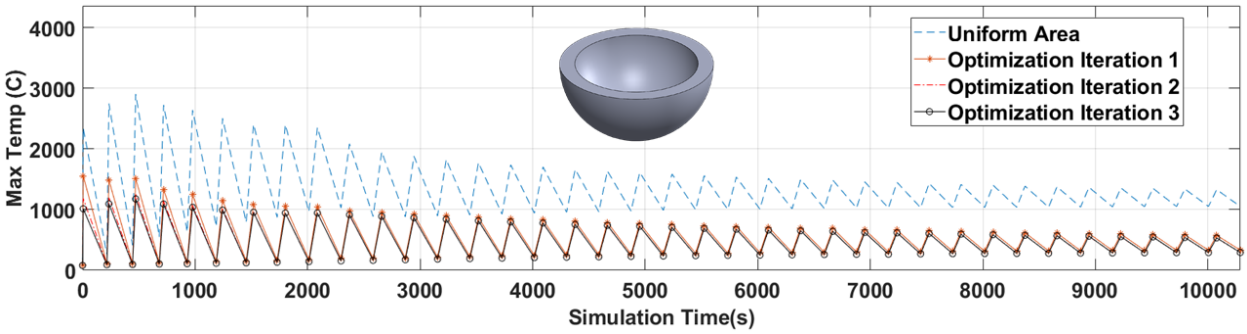

Figure 15: *Temperature cycle for un-optimized and optimized supports.*

mized truss member areas were then used to run transient thermal FEA over the coupled active systems. However, these additional rounds of optimization did not lead to significant improvement in performance as illustrated in Figure 15 for hemisphere.

The convergence of the objective function and volume constraint is illustrated in Figures 16a and 16b respectively. The optimization converges in around 80 iterations.

Similarly, for the clevis specimen, with 25% volume fraction constraint, the optimizer led to 26 % reduction in compliance. The variation of the maximum temperature for un-optimized and optimized truss-type supports is illustrated in Figure 17. Again, no significant improvement in results was obtained with additional rounds of optimization.The convergence of the objective function and constraint is shown in Figures 18a and 18b respectively.

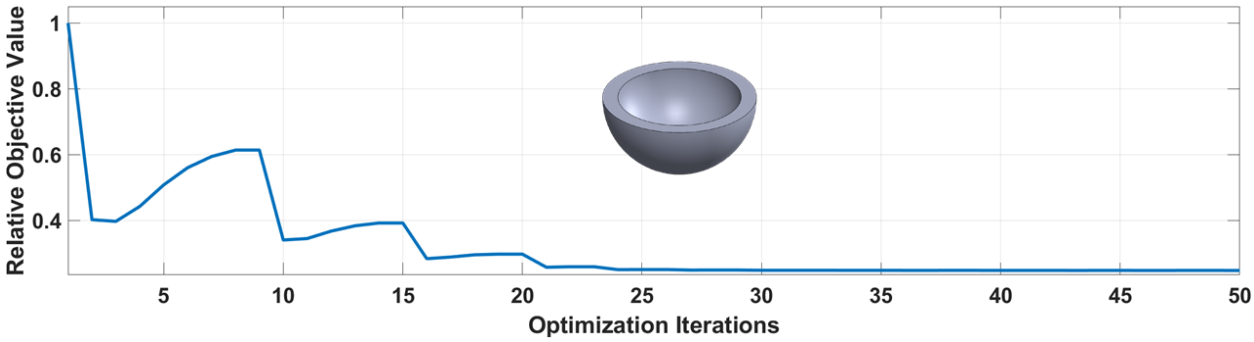

(a) *Convergence history of objective function.*

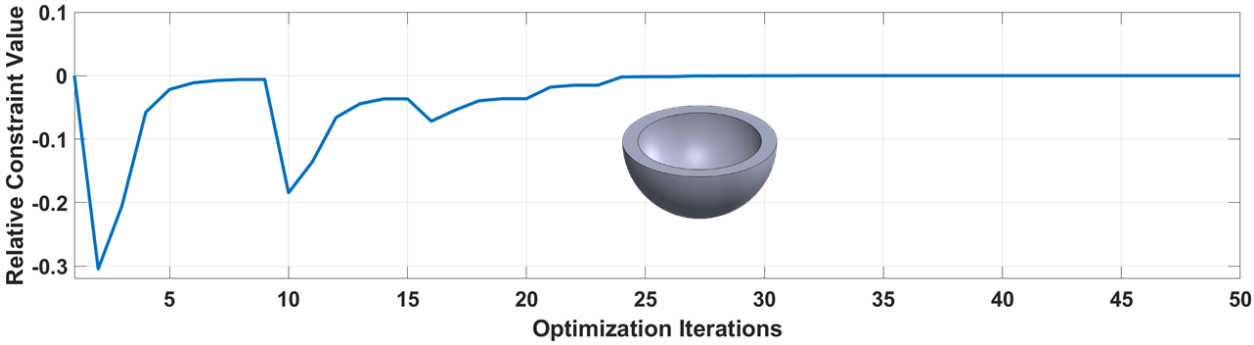

(b) *Convergence history of constraints.*

Figure 16: *Convergence history for the hemisphere.*

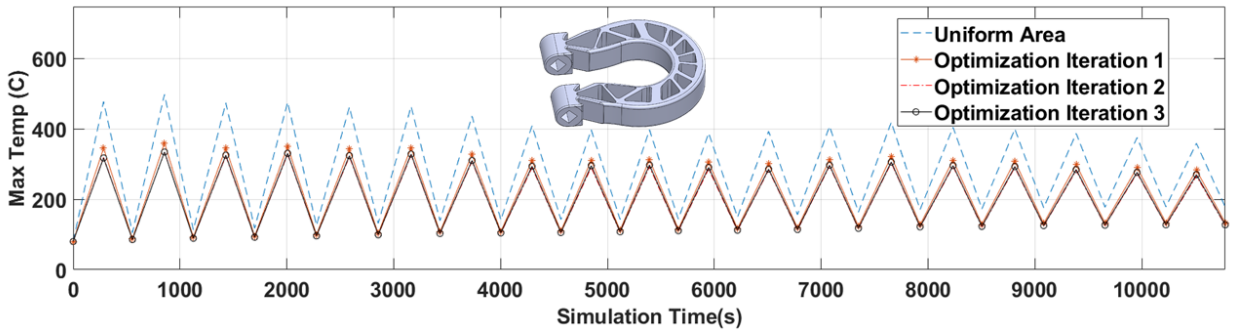

Figure 17: *Temperature cycle for un-optimized and optimized supports.*

To better visualize the optimization results, a thin half ellipse specimen is chosen as shown in Figure 19a. The truss-type support with uniform cross-section area distribution with 20% support volume fraction is shown in Figure 19b. Post-optimization, the areas of truss members change to satisfy the objective of minimizing thermal compliance as seen in Figure 19c. Material distribution concentrates along the minor-axis of half ellipse specimen based on the heat distribution in initial layers of part printing, in order to provide for larger heat transfer paths to the build plate.

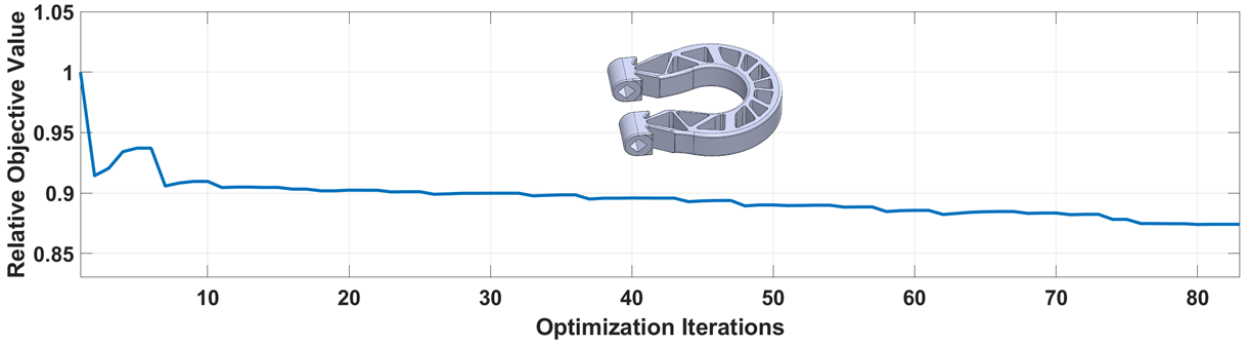

(a) *Convergence history of objective function.*

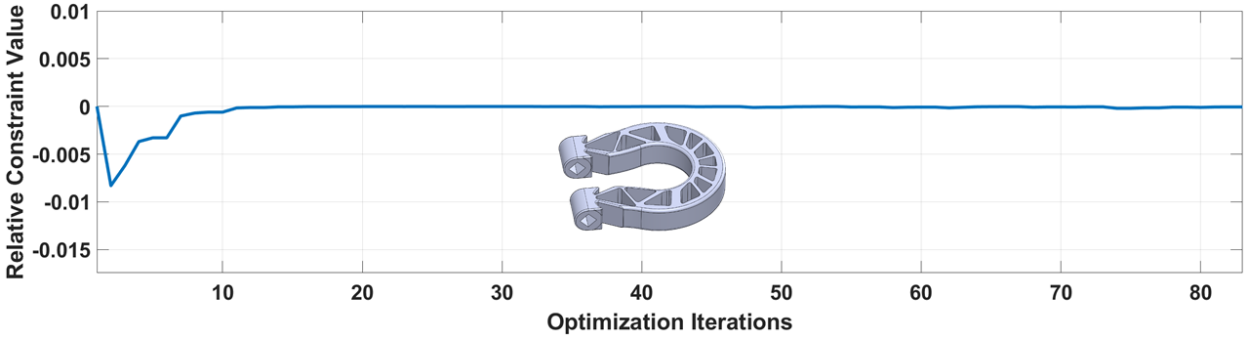

(b) *Convergence history of constraints.*

Figure 18: *Convergence history for clevis.*

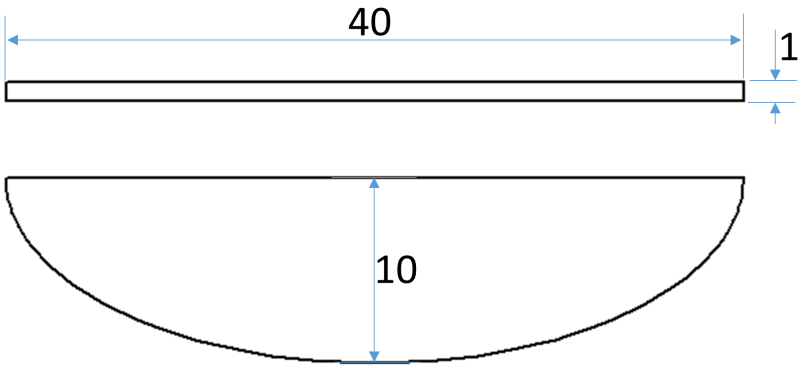

(a) *Half ellipse (units in mm).*

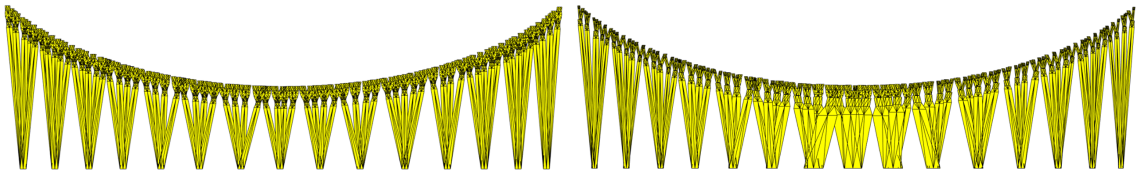

(b) *Un-optimized uniform area distribution.* (c) *Optimized area distribution.*

Figure 19: *Cross-section area optimization for half ellipse.*

5 Validation

The printability of specimens build with optimized truss-type supports was validated through manufacturing. The specimens were manufactured on an EOS-M290 machine for various support volume fractions using manufacturer recommended parameters, listed in Table 4.

Print Parameter	Units	Support Structure	Specimen
Laser Power	W	100	195
Laser Scan Speed	mm/s	675	1083
Layer Height	μm	40	20
Hatch Spacing	μm	-	90
Placement on build plate	mm	0	5

Table 4: *Print Parameters*

The truss-type supports with *un-optimized* cross-section area, printed well until printing few layers of the hemisphere specimen, validating the printability of these hybrid truss member designs. However, the edges of hemisphere suffered significant amount of burning/oxidation and warpage as seen in Figure 20, leading to part-recoater collision. These failed prints were deactivated to avoid damage to other parts.

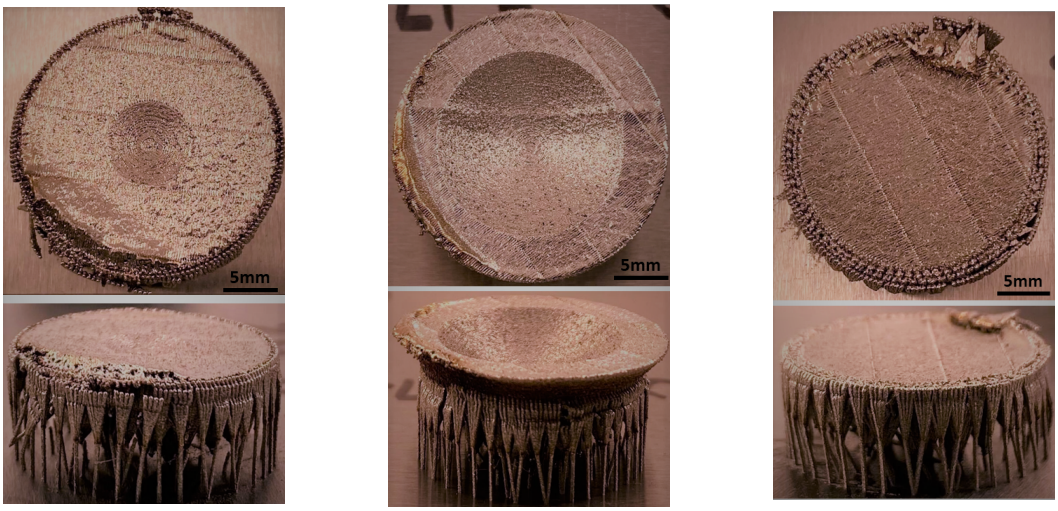

(a) *15% volume fraction.* (b) *17.5% volume fraction.* (c) *19.5% volume fraction.*

Figure 20: *Unoptimized supports for hemisphere.*

The hemisphere specimens printed with *optimized* supports are shown in Figure 21. For specimen printed with 15% and 16.4% support volume fraction, some amount of burning/oxidation was observed, but for the specimen with 17.5% support volume fraction, no such defects were observed.

(a) *15% support volume fraction.* (b) *16.4% support volume fraction.* (c) *17.5% support volume fraction.*

Figure 21: *Optimized supports for hemisphere.*

For comparison, Figure 22 shows the hemisphere specimen printed on the commonly used block-type with 16.5% (default) support volume fraction. Though perforations are added in the walled structures of the block-type support, most of the powder in the support volume, i.e., 83.5%, is entrapped that cannot be recovered. The truss-type supports, being open structured designs, do not entrap any powder, and 16.5 % is a true estimate of the support material consumed. The thin finned design also makes it easy to remove these supports from the build plate.

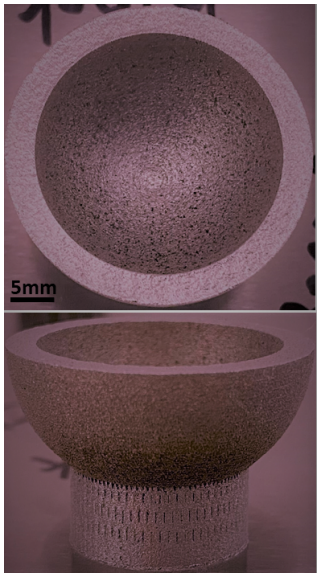

Figure 22: *Hemisphere on block-type with 16.5% support volume fraction.*

The clevis specimens printed with block-type and truss-type supports are shown in Figure 23. No defect was observed in either part printed with 25% support volume fraction. As noted earlier, the proposed truss-type support does not entrap any powder, and is easier to remove.

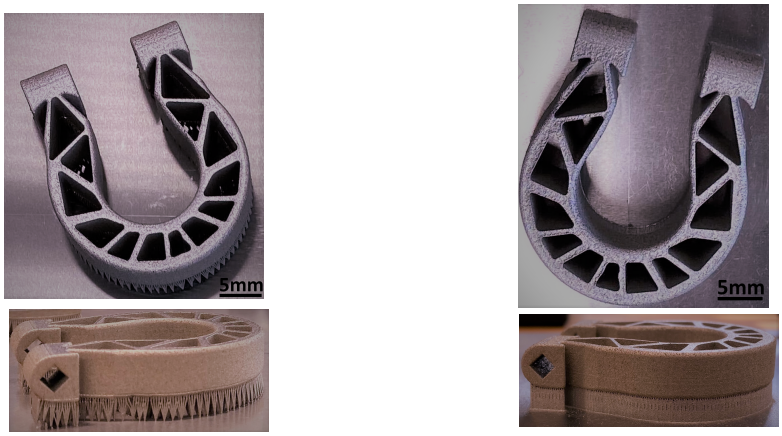

(a) *Clevis on truss-type support* (b) *Clevis on block-type support*

Figure 23: *Results for Clevis.*

6 Conclusion

This paper presents an end-to-end strategy for designing optimal support structures for LPBF. Specifically:

- A systematic and efficient strategy was presented for generating a support truss topology. The cross-section for these truss members was designed to balance thermal performance and structural strength.
- A 3D-to-1D coupled thermal framework was proposed for transient thermal simulation.
- Equivalent static loads (ESL), inspired from structural problems, were extracted from the transient simulations. These were then aggregated to pose a simple quasi-static optimization problem, with manufacturability constraints.
- Numerical results and physical validation were presented to illustrate the efficacy of the proposed framework.
- The proposed truss supports performed equally well compared to the default block-type support, with additional advantages including ease of analysis, reduced powder-wastage, and ease of removal.

Several simplifications and assumptions were made in the proposed framework, leading to possible errors:

- Equivalent-layer heating of each layer has been assumed for ease of analysis.
- For computational efficiency, meta layer thickness of 20-35 physical powder layers has been used.

- Material properties have been referenced at room temperature and assumed to be constant.

- Thermal analysis and cross-section area optimization have been performed on 1D truss members, while actual experimental prints are full 3D structures.

This is the first attempt towards optimizing truss-supports for LPBF, and several tasks and challenges lie ahead:

- Physical LPBF validation is time-consuming and expensive. This not only motivated the current work, but also limited the number of physical experiments. Additional experiments (numerical and physical) to study a variety of part geometries, materials and process parameters are necessary.

- In this work, supports were optimized for minimizing thermal compliance. Optimizing the support for minimizing the maximum temperature will need to be investigated.

- The percentage of support volume was chosen based on the recommendation from the manufacturer. Methods to predict an optimal support volume based on other failure criteria such part distortion need to be developed.

- The framework needs to be generalized for part-to-part support, with identification of optimal truss topology parameters.

- This framework needs to be extended to predict residual stresses in part.

- The microstructural properties of parts printed with different types and different amount of support needs to be investigated.

- The support topology was generated using a simple greedy algorithm. Further optimization of the support topology is desirable.

7 Acknowledgment

The specimens were printed at the Alloy Design and Development Laboratories (ADD-Lab) at the University of Wisconsin-Madison. This work was funded through Technical Data Analysis Inc. (TDA) SBIR contract #N00030-18-C-0239 and STTR contract #N68335-19-C-0321, and UW2020 WARF Discovery Institute Funds.

8 Conflict of Interest

The authors declare that there are no conflicts of interest.

References

[1] Shanshan Zhang, B Lane, J Whiting, and Kevin Chou. An investigation into metallic powder thermal conductivity in laser powder bed fusion additive manufacturing. In *Proc. Annu. Int. Solid Freefm. Fab. Symp., Austin, TX*, volume 29, pages 1796–1807, 2018.

[2] AV Gusarov and EP Kovalev. Model of thermal conductivity in powder beds. *Physical Review B*, 80(2):024202, 2009.

[3] William J Sames, FA List, Sreekanth Pannala, Ryan R Dehoff, and Sudarsanam Suresh Babu. The metallurgy and processing science of metal additive manufacturing. *International materials reviews*, 61(5):315–360, 2016.

[4] Behzad Rankouhi, Dan J Thoma, and Krishnan Suresh. Support structure design for selective laser melting process. In *Manufacturing in the Era of 4th Industrial Revolution: A World Scientific Reference Volume 1: Recent Advances in Additive Manufacturing*, pages 9–40. World Scientific, 2020.

[5] Tatiana Mishurova, Sandra Cabeza, Tobias Thiede, Naresh Nadammal, Arne Kromm, Manuela Klaus, Christoph Genzel, Christoph Haberland, and Giovanni Bruno. The influence of the support structure on residual stress and distortion in slm inconel 718 parts. *Metallurgical and materials transactions A*, 49(7):3038–3046, 2018.

[6] Katharina Bartsch, Fritz Lange, Melanie Gralow, and Claus Emmelmann. Novel approach to optimized support structures in laser beam melting by combining process simulation with topology optimization. *Journal of Laser Applications*, 31(2):022302, 2019.

[7] Jie Song, Youxiang Chew, Lishi Jiao, Xiling Yao, Seung Ki Moon, and Guijun Bi. Numerical study of temperature and cooling rate in selective laser melting with functionally graded support structures. *Additive Manufacturing*, 24:543–551, 2018.

[8] Jingchao Jiang, Xun Xu, and Jonathan Stringer. Support structures for additive manufacturing: a review. *Journal of Manufacturing and Materials Processing*, 2(4):64, 2018.

[9] Amal Charles, Ahmed Elkaseer, Lore Thijs, Veit Hagenmeyer, and Steffen Scholz. Effect of process parameters on the generated surface roughness of down-facing surfaces in selective laser melting. *Applied Sciences*, 9(6):1256, 2019.

[10] Ö Poyraz, E Yasa, G Akbulut, A Orhangul, and S Pilatin. Investigation of support structures for direct metal laser sintering (dmls) of in625 parts. In *Proceedings of the solid freeform fabrication symposium, Austin, Texas, USA*, pages 560–574, 2015.

[11] Hyeyun Song, Tom McGaughy, Alber Sadek, and Wei Zhang. Effect of structural support on microstructure of nickel base superalloy fabricated by laser-powder bed fusion additive manufacturing. *Additive Manufacturing*, 26:30–40, 2019.

[12] Naresh Nadammal, Arne Kromm, Romeo Saliwan-Neumann, Lena Farahbod, Christoph Haberland, and Pedro Dolabella Portella. Influence of support configurations on the characteristics of selective laser-melted inconel 718. *Jom*, 70(3):343–348, 2018.

[13] Martin Leary, Luigi Merli, Federico Torti, Maciej Mazur, and Milan Brandt. Optimal topology for additive manufacture: A method for enabling additive manufacture of support-free optimal structures. *Materials & Design*, 63:678–690, 2014.

[14] Yaguang Wang, Jincheng Gao, and Zhan Kang. Level set-based topology optimization with overhang constraint: Towards support-free additive manufacturing. *Computer Methods in Applied Mechanics and Engineering*, 339:591–614, 2018.

[15] Alain Garaigordobil, Rubén Ansola, Estrella Veguería, and Igor Fernandez. Overhang constraint for topology optimization of self-supported compliant mechanisms considering additive manufacturing. *Computer-Aided Design*, 109:33–48, 2019.

[16] Amir M Mirzendehdel and Krishnan Suresh. Support structure constrained topology optimization for additive manufacturing. *Computer-Aided Design*, 81:1–13, 2016.

[17] Terrence E Johnson and Andrew T Gaynor. Three-dimensional projection-based topology optimization for prescribed-angle self-supporting additively manufactured structures. *Additive Manufacturing*, 24:667–686, 2018.

[18] Minghao Bi, Phuong Tran, and Yi Min Xie. Topology optimization of 3d continuum structures under geometric self-supporting constraint. *Additive Manufacturing*, 36:101422, 2020.

[19] Paramita Das, Ramya Chandran, Rutuja Samant, and Sam Anand. Optimum part build orientation in additive manufacturing for minimizing part errors and support structures. *Procedia Manufacturing*, 1:343–354, 2015.

[20] Luca Di Angelo, Paolo Di Stefano, and Emanuele Guardiani. Search for the optimal build direction in additive manufacturing technologies: A review. *Journal of Manufacturing and Materials Processing*, 4(3):71, 2020.

[21] Giorgio Strano, L Hao, RM Everson, and KE Evans. A new approach to the design and optimisation of support structures in additive manufacturing. *The International Journal of Advanced Manufacturing Technology*, 66(9-12):1247–1254, 2013.

[22] Zhibo Luo, Fan Yang, Guoying Dong, Yunlong Tang, and Yaoyao Fiona Zhao. Orientation optimization in layer-based additive manufacturing process. In *International Design Engineering Technical Conferences and Computers and Information in Engineering Conference*, volume 50077, page V01AT02A039. American Society of Mechanical Engineers, 2016.

[23] Aaditya Chandrasekhar, Tej Kumar, and Krishnan Suresh. Build optimization of fiber-reinforced additively manufactured components. *Structural and Multidisciplinary Optimization*, 61(1):77–90, 2020.

[24] Francesco Mezzadri, Vladimir Bouriakov, and Xiaoping Qian. Topology optimization of self-supporting support structures for additive manufacturing. *Additive Manufacturing*, 21:666–682, 2018.

[25] Yang Liu, Zuyu Li, Peng Wei, and Shikui Chen. Generating support structures for additive manufacturing with continuum topology optimization methods. *Rapid Prototyping Journal*, 2019.

[26] K Mumtaz, P Vora, and N Hopkinson. A method to eliminate anchors/supports from directly laser melted metal powder bed processes. In *Proc. Solid Freeform Fabrication Symposium, Sheffield*, pages 54–64, 2011.

[27] F Calignano. Design optimization of supports for overhanging structures in aluminum and titanium alloys by selective laser melting. *Materials & Design*, 64:203–213, 2014.

[28] Lourdes D Bobbio, Shipin Qin, Alexander Dunbar, Panagiotis Michaleris, and Allison M Beese. Characterization of the strength of support structures used in powder bed fusion additive manufacturing of ti-6al-4v. *Additive Manufacturing*, 14:60–68, 2017.

[29] Lin Zhu, Ruiliang Feng, Juntong Xi, Peng Li, and Xiangzhi Wei. A lightweight design of tree-shaped support structures for slm additive manufacturing. *Comput. Aided Des. Appl*, 17:716–726, 2020.

[30] Zhiping Wang, Yicha Zhang, Shujie Tan, Liping Ding, and Alain Bernard. Support point determination for support structure design in additive manufacturing. *Additive Manufacturing*, 47:102341, 2021.

[31] Benjamin Vaissier, Jean-Philippe Pernot, Laurent Chougrani, and Philippe Véron. Genetic-algorithm based framework for lattice support structure optimization in additive manufacturing. *Computer-Aided Design*, 110:11–23, 2019.

[32] Yicha Zhang, Zhiping Wang, Yancheng Zhang, Samuel Gomes, and Alain Bernard. Bio-inspired generative design for support structure generation and optimization in additive manufacturing (am). *CIRP Annals*, 69(1):117–120, 2020.

[33] John G Michopoulos, Samuel Lambrakos, and Athanasios Iliopoulos. Multiphysics challenges for controlling layered manufacturing processes targeting thermomechanical performance. In *International Design Engineering Technical Conferences and Computers and Information in Engineering Conference*, volume 46285, page V01AT02A050. American Society of Mechanical Engineers, 2014.

[34] Richard Martukanitz, Pan Michaleris, Todd Palmer, Tarasankar DebRoy, Zi-Kui Liu, Richard Otis, Tae Wook Heo, and Long-Qing Chen. Toward an integrated computational system for describing the additive manufacturing process for metallic materials. *Additive Manufacturing*, 1:52–63, 2014.

[35] Anirudh Krishnakumar, Krishnan Suresh, and Aaditya Chandrasekar. Towards assembly-free methods for additive manufacturing simulation. In *International Design Engineering Technical Conferences and Computers and Information in Engineering Conference*, volume 57045, page V01AT02A021. American Society of Mechanical Engineers, 2015.

[36] Ahmed Hussein, Liang Hao, Chunze Yan, and Richard Everson. Finite element simulation of the temperature and stress fields in single layers built without-support in selective laser melting. *Materials & Design (1980-2015)*, 52:638–647, 2013.

[37] Hong-Chuong Tran and Yu-Lung Lo. Heat transfer simulations of selective laser melting process based on volumetric heat source with powder size consideration. *Journal of Materials Processing Technology*, 255:411–425, 2018.

[38] Ali Foroozmehr, Mohsen Badrossamay, Ehsan Foroozmehr, and Sa'id Golabi. Finite element simulation of selective laser melting process considering optical penetration depth of laser in powder bed. *Materials & Design*, 89:255–263, 2016.

[39] Yingli Li, Kun Zhou, Shu Beng Tor, Chee Kai Chua, and Kah Fai Leong. Heat transfer and phase transition in the selective laser melting process. *International Journal of Heat and Mass Transfer*, 108:2408–2416, 2017.

[40] Kurian Antony, N Arivazhagan, and K Senthilkumaran. Numerical and experimental investigations on laser melting of stainless steel 316l metal powders. *Journal of Manufacturing Processes*, 16(3):345–355, 2014.

[41] Daniel Rosenthal. The theory of moving sources of heat and its application of metal treatments. *Transactions of ASME*, 68:849–866, 1946.

[42] M Labudovic, D Hu, and R Kovacevic. A three dimensional model for direct laser metal powder deposition and rapid prototyping. *Journal of materials science*, 38(1):35–49, 2003.

[43] Y Yang, MF Knol, F Van Keulen, and C Ayas. A semi-analytical thermal modelling approach for selective laser melting. *Additive Manufacturing*, 21:284–297, 2018.

[44] PJ Cheng and SC Lin. An analytical model for the temperature field in the laser forming of sheet metal. *Journal of Materials Processing Technology*, 101(1-3):260–267, 2000.

[45] Yuze Huang, Mir Behrad Khamesee, and Ehsan Toyserkani. A comprehensive analytical model for laser powder-fed additive manufacturing. *Additive Manufacturing*, 12:90–99, 2016.

[46] Maarten Van Elsen, Martine Baelmans, Peter Mercelis, and J-P Kruth. Solutions for modelling moving heat sources in a semi-infinite medium and applications to laser material processing. *International Journal of heat and mass transfer*, 50(23-24):4872–4882, 2007.

[47] DQ Zhang, QZ Cai, JH Liu, L Zhang, and RD Li. Select laser melting of w–ni–fe powders: simulation and experimental study. *The International Journal of Advanced Manufacturing Technology*, 51(5-8):649–658, 2010.

[48] Bo Song, Shujuan Dong, Hanlin Liao, and Christian Coddet. Process parameter selection for selective laser melting of ti6al4v based on temperature distribution simulation and experimental sintering. *The International Journal of Advanced Manufacturing Technology*, 61(9):967–974, 2012.

[49] Kai Zeng, Deepankar Pal, Chong Teng, and Brent E Stucker. Evaluations of effective thermal conductivity of support structures in selective laser melting. *Additive Manufacturing*, 6:67–73, 2015.

[50] Xuan Liang, Wen Dong, Shawn Hinnebusch, Qian Chen, Hai T Tran, John Lemon, Lin Cheng, Zekai Zhou, Devlin Hayduke, and Albert C To. Inherent strain homogenization for fast residual deformation simulation of thin-walled lattice support structures built by laser powder bed fusion additive manufacturing. *Additive Manufacturing*, 32:101091, 2020.

[51] Ibiye Aseibichin Roberts, CJ Wang, R Esterlein, M Stanford, and DJ Mynors. A three-dimensional finite element analysis of the temperature field during laser melting of metal powders in additive layer manufacturing. *International Journal of Machine Tools and Manufacture*, 49(12-13):916–923, 2009.

[52] Kai Zeng. *Optimization of support structures for selective laser melting*. PhD thesis, 2015.

[53] TA Krol, F Zach, and C Seidel. Optimization of supports in metal-based additive manufacturing by means of finite element models. In *2012 International Solid Freeform Fabrication Symposium*. University of Texas at Austin, 2012.

[54] Dengyang Zhao, Ming Li, and Yusheng Liu. A novel application framework for self-supporting topology optimization. *The Visual Computer*, 37(5):1169–1184, 2021.

[55] Emiel van de Ven, Can Ayas, Matthijs Langelaar, Robert Maas, and Fred van Keulen. Accessibility of support structures in topology optimization for additive manufacturing. *International Journal for Numerical Methods in Engineering*, 122(8):2038–2056, 2021.

[56] Matthijs Langelaar. Topology optimization for additive manufacturing with controllable support structure costs. In *7th European Congress on Computational Methods in Applied Sciences and Engineering*, pages 3689–3699. National Technical University of Athens (NTUA), Greece, 2016.

[57] Xiaoping Qian. Undercut and overhang angle control in topology optimization: a density gradient based integral approach. *International Journal for Numerical Methods in Engineering*, 111(3):247–272, 2017.

[58] Grégoire Allaire and Beniamin Bogosel. Optimizing supports for additive manufacturing. *Structural and Multidisciplinary Optimization*, 58(6):2493–2515, 2018.

[59] Eilam Amir and Oded Amir. Concurrent high-resolution topology optimization of structures and their supports for additive manufacturing. *Structural and Multidisciplinary Optimization*, 63(6):2589–2612, 2021.

[60] Mingdong Zhou, Yichang Liu, and Zhongqin Lin. Topology optimization of thermal conductive support structures for laser additive manufacturing. *Computer Methods in Applied Mechanics and Engineering*, 353:24–43, 2019.

[61] Jeroen Pellens, Geert Lombaert, Manuel Michiels, Tom Craeghs, and Mattias Schevenels. Topology optimization of support structure layout in metal-based additive manufacturing accounting for thermal deformations. *Structural and Multidisciplinary Optimization*, 61(6):2291–2303, 2020.

[62] Cunfu Wang and Xiaoping Qian. Optimizing support for heat dissipation in additive manufacturing. In *International Design Engineering Technical Conferences and Computers and Information in Engineering Conference*, volume 83983, page V009T09A018. American Society of Mechanical Engineers, 2020.

[63] Umberto Paggi, Rajit Ranjan, Lore Thijs, Can Ayas, Matthijs Langelaar, Fred van Keulen, and Brecht van Hooreweder. New support structures for reduced overheating on downfacing regions of direct metal printed parts. In *30th Annual International Solid Freeform Fabrication Symposium; University of Texas: Austin, TX, USA*, 2019.

[64] Yu-Hsin Kuo, Chih-Chun Cheng, Yang-Shan Lin, and Cheng-Hung San. Support structure design in additive manufacturing based on topology optimization. *Structural and Multidisciplinary Optimization*, 57(1):183–195, 2018.

[65] Kang-Hyun Lee and Gun Jin Yun. Design optimization of thermally conductive support structure for laser powder-bed fusion process with part-scale thermal history. *Additive Manufacturing*, page 102627, 2022.

[66] Lin Cheng, Xuan Liang, Jiaxi Bai, Qian Chen, John Lemon, and Albert To. On utilizing topology optimization to design support structure to prevent residual stress induced build failure in laser powder bed metal additive manufacturing. *Additive Manufacturing*, 27:290–304, 2019.

[67] Renkai Huang, Ning Dai, Xiaosheng Cheng, and Lei Wang. Topology optimization of lattice support structures for heat conduction in selective laser melting. *The International Journal of Advanced Manufacturing Technology*, 109(7):1841–1851, 2020.

[68] Takao Miki and Shinji Nishiwaki. Topology optimization of the support structure for heat dissipation in additive manufacturing. *Finite Elements in Analysis and Design*, 203:103708, 2022.

[69] Subodh C Subedi, Chaman Singh Verma, and Krishnan Suresh. A review of methods for the geometric post-processing of topology optimized models. *Journal of Computing and Information Science in Engineering*, 20(6), 2020.

[70] Michael Gouge, Erik Denlinger, Jeff Irwin, Chao Li, and Pan Michaleris. Experimental validation of thermo-mechanical part-scale modeling for laser powder bed fusion processes. *Additive Manufacturing*, 29:100771, 2019.

[71] Michael F Zaeh and Gregor Branner. Investigations on residual stresses and deformations in selective laser melting. *Production Engineering*, 4(1):35–45, 2010.

[72] Changpeng Chen, Shijie Chang, Junjie Zhu, Zhongxu Xiao, Haihong Zhu, and Xiaoyan Zeng. Residual stress of typical parts in laser powder bed fusion. *Journal of Manufacturing Processes*, 59:621–628, 2020.

[73] Juraj Vanek, Jorge A Garcia Galicia, and Bedrich Benes. Clever support: Efficient support structure generation for digital fabrication. In *Computer graphics forum*, volume 33, pages 117–125. Wiley Online Library, 2014.

[74] Yong Zhou, Han Lu, Qingrong Ren, and Yang Li. Generation of a tree-like support structure for fused deposition modelling based on the l-system and an octree. *Graphical Models*, 101:8–16, 2019.

[75] Andrés Díaz Lantada, Adrián de Blas Romero, Álvaro Sánchez Isasi, and Diego Garrido Bellido. Design and performance assessment of innovative eco-efficient support structures for additive manufacturing by photopolymerization. *Journal of Industrial Ecology*, 21(S1):S179–S190, 2017.

[76] S Weber, J Montero, M Bleckmann, and K Paetzold. Parameters on support structure design for metal additive manufacturing. In *Proceedings of the Design Society: DESIGN Conference*, volume 1, pages 1145–1154. Cambridge University Press, 2020.

[77] Yuchu Qin, Qunfen Qi, Paul J Scott, and Xiangqian Jiang. Determination of optimal build orientation for additive manufacturing using muirhead mean and prioritised average operators. *Journal of Intelligent Manufacturing*, 30(8):3015–3034, 2019.

[78] Milan Dana, Ivana Zetkova, and Pavel Hanzl. Need for support structures depending on overhang size. *MM Science Journal*, pages 1597–1601, 2016.

[79] Yicha Zhang and Alain Bernard. Generic build time estimation model for parts produced by sls. In *High value manufacturing: Advanced research in virtual and rapid prototyping. Proceedings of the 6th International Conference on Advanced Research in Virtual and Rapid Prototyping*, pages 43–48, 2013.

[80] Saish Tedia and Christopher B Williams. Manufacturability analysis tool for additive manufacturing using voxel-based geometric modeling. In *27th annual international solid freeform fabrication (SFF) symposium*, pages 3–22, 2016.

[81] Thomas Mayer, Gabriel Brändle, Andreas Schönenberger, and Robert Eberlein. Simulation and validation of residual deformations in additive manufacturing of metal parts. *Heliyon*, 6(5):e03987, 2020.

[82] Jinqiang Ning, Daniel E Sievers, Hamid Garmestani, and Steven Y Liang. Analytical thermal modeling of metal additive manufacturing by heat sink solution. *Materials*, 12(16):2568, 2019.

[83] MR Frewin and DA Scott. Finite element model of pulsed laser welding. *WELDING JOURNAL-NEW YORK-*, 78:15–s, 1999.

[84] Yingli Li, Kun Zhou, Pengfei Tan, Shu Beng Tor, Chee Kai Chua, and Kah Fai Leong. Modeling temperature and residual stress fields in selective laser melting. *International Journal of Mechanical Sciences*, 136:24–35, 2018.

[85] L Papadakis, A Loizou, J Risse, and J Schrage. Numerical computation of component shape distortion manufactured by selective laser melting. *Procedia Cirp*, 18:90–95, 2014.

[86] P Prabhakar, William J Sames, R Dehoff, and Sudarsanam Suresh Babu. Computational modeling of residual stress formation during the electron beam melting process for inconel 718. *Additive Manufacturing*, 7:83–91, 2015.

[87] Mohamad Bayat, Christopher G Klingaa, Sankhya Mohanty, David De Baere, Jesper Thorborg, Niels S Tiedje, and Jesper H Hattel. Part-scale thermo-mechanical modelling of distortions in laser powder bed fusion–analysis of the sequential flash heating method with experimental validation. *Additive Manufacturing*, 36:101508, 2020.

[88] Mohamad Bayat, Wen Dong, Jesper Thorborg, Albert C To, and Jesper H Hattel. A review of multi-scale and multi-physics simulations of metal additive manufacturing processes with focus on modelling strategies. *Additive Manufacturing*, page 102278, 2021.

[89] Joaquim Ciurana, Luis Hernandez, and Jordi Delgado. Energy density analysis on single tracks formed by selective laser melting with cocrmo powder material. *The International Journal of Advanced Manufacturing Technology*, 68(5-8):1103–1110, 2013.

[90] Umberto Scipioni Bertoli, Alexander J Wolfer, Manyalibo J Matthews, Jean-Pierre R Delplanque, and Julie M Schoenung. On the limitations of volumetric energy density as a design parameter for selective laser melting. *Materials & Design*, 113:331–340, 2017.

[91] Jingsheng Wang, Jiajia Zhang, Lvjie Liang, Anguo Huang, Guang Yang, and Shengyong Pang. A line-based flash heating method for numerical modeling and prediction of directed energy deposition manufacturing process. *Journal of Manufacturing Processes*, 73:822–838, 2022.

[92] Nathan M Newmark. A method of computation for structural dynamics. *Journal of the engineering mechanics division*, 85(3):67–94, 1959.

[93] Robert D Cook et al. *Concepts and applications of finite element analysis*. John wiley & sons, 2007.

[94] Woo-Seok Choi, Keun-Bae Park, and Gyung-Jin Park. Calculation of equivalent static loads and its application. *Nuclear engineering and design*, 235(22):2337–2348, 2005.

[95] Vivek Ganeshan and Sushanth Shandilya Dattakumar. Converting dynamic impact events to equivalent static loads in vehicle chassis (master's thesis). Master's thesis, 2017.

[96] Gyung-Jin Park. Equivalent static loads method for non linear static response structural optimization. In *9th LS-DYNA German User's Forum, Bamberg, Germany*, 2010.

[97] Woo-Seok Choi and GJ Park. Transformation of dynamic loads into equivalent static loads based on modal analysis. *International Journal for Numerical Methods in Engineering*, 46(1):29–43, 1999.

[98] Sang-ok Park, Wook-Han Choi, and Gyung-Jin Park. Dynamic response optimization of structures with viscoelastic material using the equivalent static loads method. *Proceedings of the Institution of Mechanical Engineers, Part D: Journal of Automobile Engineering*, 235(2-3):589–603, 2021.

[99] JY Zhang, Makoto Ohsaki, and Atsushi Uchida. Equivalent static loads for nonlinear seismic design of spatial structures. In *Proc. 14th World Conf. on Earthquake Eng*, 2008.

[100] Hwan-Hak Jang, HA Lee, JY Lee, and GJ Park. Dynamic response topology optimization in the time domain using equivalent static loads. *AIAA journal*, 50(1):226–234, 2012.

[101] SI Yi, JY Lee, and GJ Park. Crashworthiness design optimization using equivalent static loads. *Proceedings of the Institution of Mechanical Engineers, Part D: Journal of automobile engineering*, 226(1):23–38, 2012.

[102] Krister Svanberg. A globally convergent version of mma without linesearch. In *Proceedings of the first world congress of structural and multidisciplinary optimization*, volume 28, pages 9–16. Goslar, Germany, 1995.

[103] Juan J Valencia and Peter N Quested. Thermophysical properties. *ASM Handbook*, 15:468 – 481, 2013.

[104] Behzad Rankouhi, Ankur Kumar Agrawal, Frank E Pfefferkorn, and Dan J Thoma. A dimensionless number for predicting universal processing parameter boundaries in metal powder bed additive manufacturing. *Manufacturing Letters*, 27:13–17, 2021.